von Karman Institute for Fluid Dynamics

Lecture Series 2025-01

MEASUREMENT, MODELLING AND SIMULATIONS TECHNIQUES FOR NOVEL AIRCRAFT ARCHITECTURES

November 4-6, 2024

AERODYNAMIC AND AEROACOUSTIC OPTIMIZATION OF DISTRIBUTED ELECTRIC PROPULSION SYSTEMS

R. Ballano Martinez[1]; M. Andrejasic[1]; J. Christophe[2]
[1]Pipistrel Vertical Solutions d.o.o., Slovenia
[2]von Karman Institute for Fluid Dynamics, Belgium

Aerodynamic and aeroacoustic optimization of Distributed Electric Propulsion systems

Roman Ballano Martinez [a] Matej Andrejasic [b]
Pipistrel Vertical Solutions d.o.o., Slovenia

Julien Christophe [c]
von Karman Institute for Fluid Dynamics

6 November 2024

Contents

1 Introduction **3**

2 Optimization toolchain **5**
2.1 Geometry 5
2.1.1 Single propeller mesh study 5
2.2 Aerodynamic modelling 7
2.3 Aeroacoustic prediction solvers 7
2.3.1 Tonal acoustic solver 8
2.3.2 Trailing-edge broadband acoustic solver 9
2.3.3 Example of aeroacoustic predictions 10
2.4 Optimizer 11

3 Optimization results **13**
3.1 Baseline design 13
3.2 Methodology 13
3.3 Results 15

4 Conclusions **19**

[a] Aerodynamics Engineer, Pipistrel Vertical Solutions, roman.ballano@pipistrel-aircraft.com
[b] Manager of Flight Physics and Simulations department, matej.andrejasic@pipistrel-aircraft.com
[c] Research Expert, julien.christophe@vki.ac.be

1 Introduction

Distributed propulsion (DP) solutions have gained attention in aviation due to their potential benefits in terms of performance but also in terms of noise reduction, as indicated in previous studies [1, 2, 3, 4]. While DP systems involve complex aerodynamic interactions that might initially suggest increased noise, several factors offer promising opportunities for noise mitigation. As an example, the positive aerodynamic effects of wing blowing result is higher lift-to-drag ratios allowing for steeper take-off and landing trajectories that lower the overall noise footprint. Additionally, the ability to optimize the propeller geometry and reduce interactions through strategic placement of propellers opens new possibilities for minimizing tonal and broadband noise and improving community noise impact. To fully exploit these benefits, it is essential to consider the intricate balance between aero-propulsive efficiency, noise mitigation techniques, and interference effects.

In the present notes, a low-fidelity framework for the analysis and optimization of distributed electric propulsion (DEP) systems has been established using a chain composed of an open-source parametric geometry engine (OpenVSP), a low-fidelity unsteady three-dimensional panel code (FlightStream) and semi-analytical tonal and broadband noise estimation models ($BATMAN^{\pi}$). The desired aerodynamic and acoustic performance metrics of the modelled systems are transferred to an optimization hypervisor (modeFRONTIER) which manages changes in geometrical parameters to achieve an optimal design.

The use of low fidelity and semi-analytical models allows for this optimization chain to be run on modest hardware such as individual workstations, facilitating the incorporation of optimization procedures in early design stages. An overview of the framework can be seen in Figure 1.

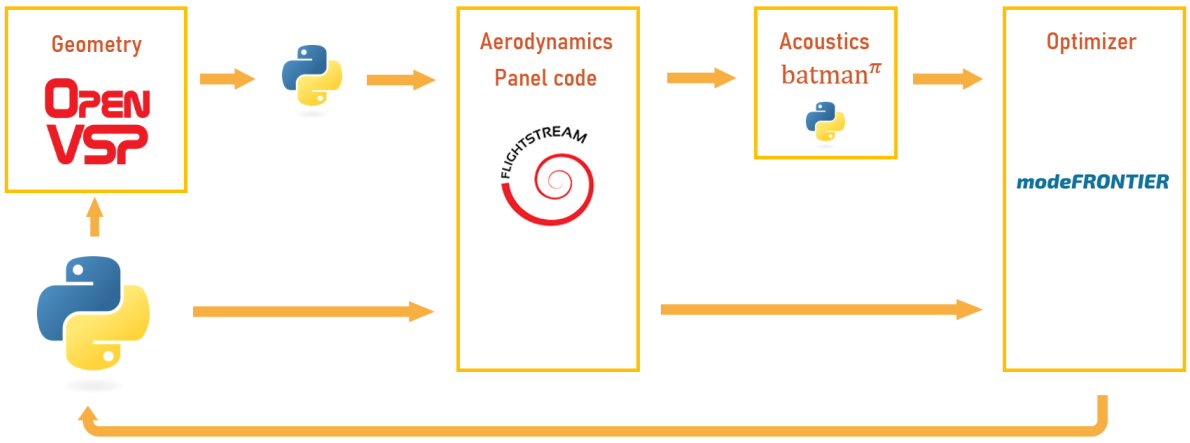


Figure 1: Block diagram of the DEP optimization framework.

2 Optimization toolchain

2.1 Geometry

The geometry engine used in this framework is OpenVSP [5, 6], an open-source vehicle design tool with a focus on parametrically defined elements. Propeller geometries are created through sectional shapes (airfoils) and twist, sweep and chord distributions, using spline-based interpolation between the specified section data. Wings and control surfaces are defined similarly. Mesh settings can be controlled parametrically, generating structured surface meshes like the one seen in Figure 2.

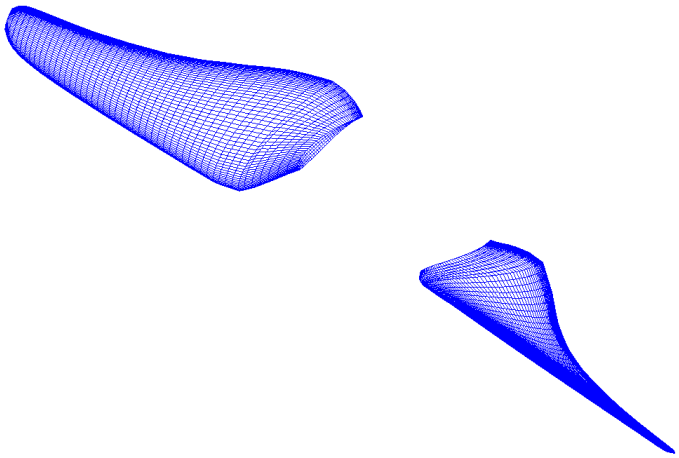


Figure 2: Sample propeller surface mesh.

2.1.1 Single propeller mesh study

A preliminary mesh study has been carried out on a single propeller and wing configuration. The aim was to determine an adequate mesh resolution to use in the final multi-propeller optimization procedure that brings a high enough level of accuracy without increasing computational cost unreasonably. The test case consists of a two bladed, 1.5 meter diameter propeller with chord, twist and rake variations in front of a 3 meter span, straight wing with a NACA0014 airfoil, which can also be seen in Figure 3.

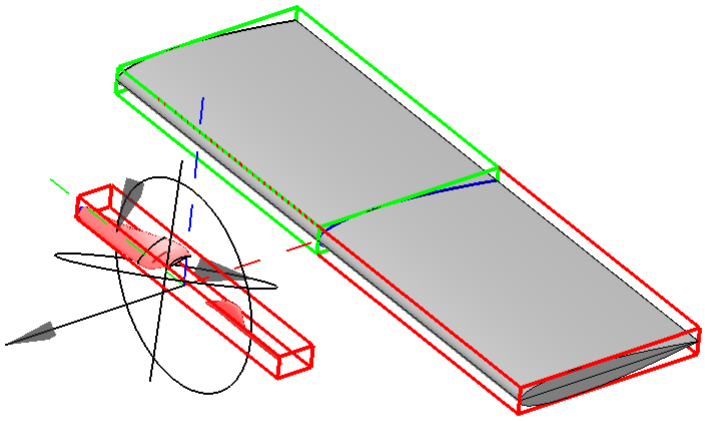


Figure 3: Single propeller-wing configuration.

Due to the lack of experimental data for this simplified setup, an angle of attack of $\alpha = 0°$ has been set in order to aim at obtaining a zero mean lift coefficient $\bar{C}_L$ on the symmetrical wing over the last four revolutions.

Figure 4 shows the mean C_L and runtime results for five different mesh element counts, normalized with the coarsest mesh number of elements. A good compromise between accuracy and runtime has been found for a mesh consisting of 45 spanwise and 40 chordwise elements for the wing and 20 spanwise and 50 chordwise elements for each of the propeller blades. This resolution was later used for the main optimization procedure.

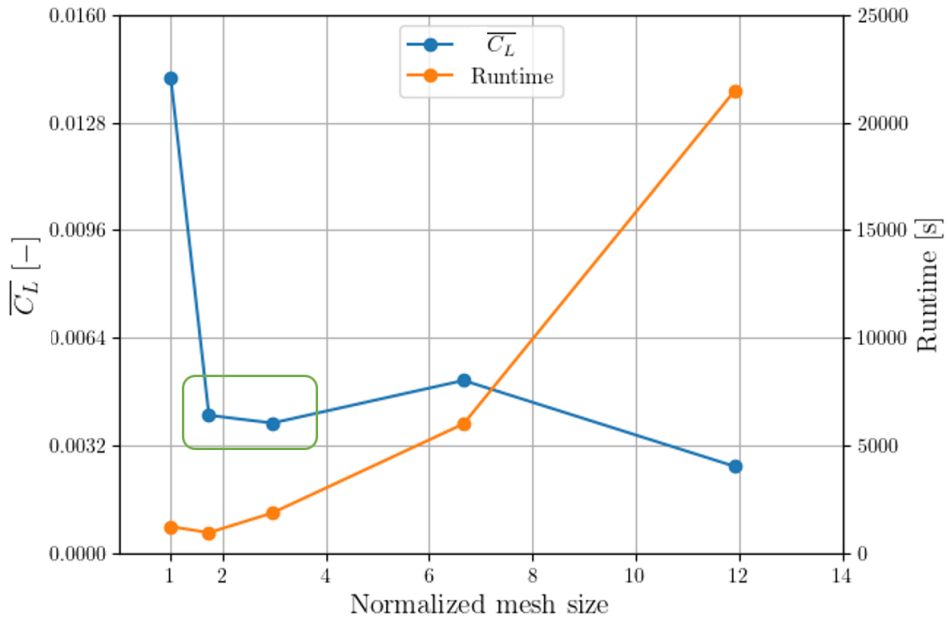


Figure 4: Runtime and result comparison between the five analyzed meshes.

2.2 Aerodynamic modelling

Unsteady aerodynamic characteristics of the propeller-wing system is computed using the three dimensional, viscous coupled panel code FlightStream [7, 8]. This solver combines a surface vorticity formulation with integral boundary layer methods, allowing for the vortex sheet wake based modelling of the propeller-wing interaction.

Applicable take-off flight regimes for DEP systems are away from stall regions and, thus, key phenomena should be captured by panel methods and integral boundary layer theory.

Figure 5 shows an instantaneous snapshot of pressure coefficient (C_p) contours for a sample multi-propeller setup and a constant chord wing with a symmetrical airfoil, at zero angle of attack. The effect of the wakes on the wings is visible through a local increase in angle of attack and thus a reduction in peak upper surface C_p on the advancing blade side, and a reduction on the retreating blade side.

Surface pressure and boundary layer thickness results for the propeller blades are then used as inputs for the tonal and broadband noise acoustics models, constituting a postprocessing step after the aerodynamic simulation finishes.

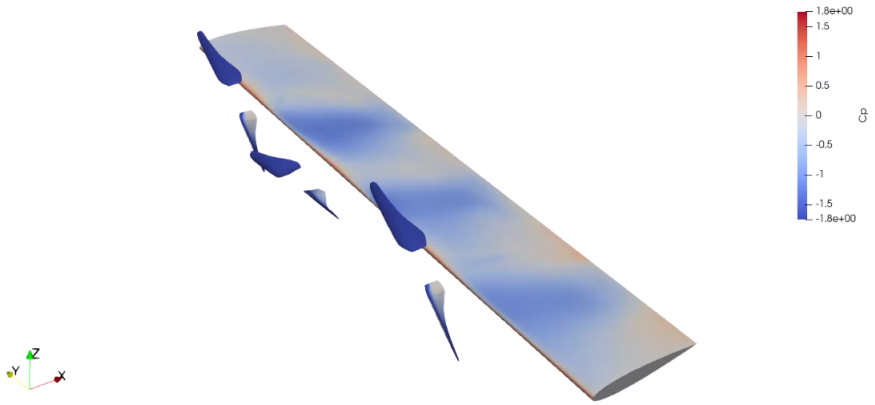


Figure 5: Instantaneous pressure coefficient contours for a three-propeller configuration.

2.3 Aeroacoustic prediction solvers

A number of noise generation mechanisms are expected in tractor DEP configurations, listed in Figure 6. At low Mach numbers and for frequencies low enough to make each source acoustically compact, noise production is intimately associated to the unsteady forces exerted by the solid surfaces on the surrounding fluid, either due to two-body interactions, or to mechanisms that are intrinsic to a given component.

The *self-noise* category includes the noise emitted by the turbulent boundary layer of the blade or wing when it reaches the trailing-edge [9, 10]. This mechanism usually contributes to the broadband part of the sound spectrum, owing to the broad range of turbulent scales that are found in a fully developed turbulent boundary layer. In the case of propellers, two other self-noise mechanisms are due to the centrifugal acceleration of the steady forces, causing *steady loading noise*, and to the displacement of fluid by the blade motion, leading to the so-called *thickness noise* [11]. Both mechanisms, being periodic by nature, contribute to the tonal content of the noise spectrum.

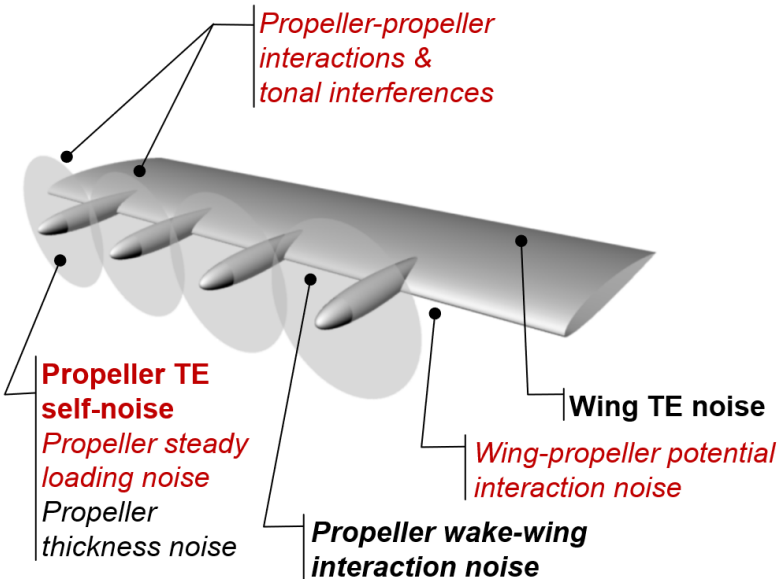


Figure 6: Tonal (italic) and broadband (bold) noise generation mechanisms. Those indicated in red are modelled in the present study.

The two-body aerodynamic interactions can be distinguished as *viscous interaction* and *potential interaction* [12]. The first instance corresponds to the wake of the propeller blade inducing unsteady forces on the wing. Those viscous interaction mechanisms are associated with both tonal and broadband noise, due to the turbulence that is advected within the wake. Potential interaction induces tonal noise when the distance between the two involved components is small enough, typically of the order of a couple of radii of curvature of the leading edge of the downstream element. Similarly, when two propellers are separated by small lateral distances, potential interactions can create additional tonal noise.

In the present acoustic module, implemented in $BATMAN^{\pi}$, the input data is taken from the panel code Flightstream. It allows to take into account flow non-uniformities along the propeller rotation and potential interactions (propeller-propeller and propeller-wing), both contributing to tonal noise. Thanks to the boundary-layer model, it also provides the inputs to the broadband noise models as detailed below. Beyond the aerodynamic installation effects, acoustic installation effects are also present when the noise is reflected by the airframe. Those effects are neglected at this stage. Furthermore, the loads on the main wing would deserve further investigations to determine their accuracy. The corresponding noise mechanisms are then also neglected. All the mechanisms taken into account in the model are shown in red in Figure 6.

2.3.1 Tonal acoustic solver

The present methodology uses the formalism of the Ffowcs Williams-Hawkings (FWH) analogy [13] to predict the tonal noise emissions. Given the tip Mach number ($M_{\text{tip}} \approx 0.5$) and the acoustic compactness of the blades for the first BPFs, the contributions of the quadrupolar and thickness noise have been omitted [14]. The tonal noise is then associated with the steady and periodic components of the blade forces, considered as equivalent rotating dipoles [15, 16]. The

acoustic pressure in the geometric field-field of each propeller is given by:

$$p_{nB} \simeq -\frac{\mathrm{i}Bk_{nB}}{4\pi}\frac{\mathrm{e}^{-ik_{nB}x}}{x} \sum_{p=-\infty}^{+\infty} \mathrm{e}^{-i(nB-p)(\varphi-\pi/2)}\mathrm{J}_{-nB+p}\left(-k_{nB}R_0\sin\theta\right)\left[F_p^{(T)}\cos\theta - \frac{nB-p}{k_{nB}R_0}F_p^{(D)}\right] \quad (1)$$

for the n-th harmonic of the BPF, B is the number of blades, $k_{nB} = nB\Omega/c_0$ with Ω the propeller angular frequency, x is the listener distance and R_0 is the radius where the force is applied. φ and θ are the listener's azimuthal and polar angles, respectively. $F_p^{(T)}$ and $F_p^{(D)}$ are the p-th harmonics of the thrust and drag, respectively, exerted by each blade of our propellers on the fluid. Further details and explanations are given in [14]

In the numerical implementation of this equation, the BLHs are integrated over small segments dividing the blade surface in the spanwise and chordwise directions. Those segments, also called strips, must be *i*) acoustically compact and *ii*) small enough to resolve the spanwise and chordwise variations of the amplitude and phase of the equivalent dipoles borne by each strip. In the present study, each blade has been divided into 7 sections in the spanwise direction and into 2 sections in the chordwise direction.

The above theory has been implemented in the in-house Python-based solver BATMAN$^\pi$ (Broadband And Tonal Models for Airfoil Noise).

2.3.2 Trailing-edge broadband acoustic solver

A semi-analytical model is provided by Amiet [17] to compute the broadband trailing-edge noise for an isolated airfoil. Since the model is based on a linearized gust-airfoil response, the airfoil is assumed to have negligible thickness, camber and angle-of-attack. Assuming that the chord is infinite in the upstream direction, the main trailing-edge scattering is obtained as a solution of a Schwartzchild problem [17], which was further extended by applying a leading-edge back-scattering correction to account for finite-chord effects [10]. The radiated sound field is calculated by integrating the induced surface sources on the actual chord length $c = 2b$, and the airfoil span $L = 2d$, assuming convection of frozen turbulence past the trailing edge. For large airfoil aspect ratio (L/c), the Power Spectral Density (PSD) of the sound pressure in the geometrical far field is obtained as:

$$S_{pp}(\mathbf{x},\omega) = \left(\frac{kzb}{\pi\sigma_0}\right)^2 d\,|\mathcal{L}(\mathbf{x},K_x,K_y)|^2\,\phi_{pp}(\omega)\,l_y(\omega,K_y) \quad (2)$$

where $\mathbf{x} = (x,y,z)$ is the observer position as defined in Figure 7, $k = \omega/c_0$ is the wavenumber, with ω the angular frequency and c_0 the speed of sound. σ_0 is the airfoil-listener distance corrected for convection effects. K_x and K_y are gust wavenumbers defined as $K_y = ky/\sigma_0$, and $K_x = \omega/U_c$ where U_c is the convection velocity past the trailing-edge. l_y is the spanwise correlation length, ϕ_{pp} is the wall-pressure spectrum, $\mathcal{L} = \mathcal{L}_1 + \mathcal{L}_2$ is the aeroacoustic transfer function [10] for the main contribution term from the trailing-edge, $\mathcal{L}_1$, and the leading edge back-scattering term, $\mathcal{L}_2$. In the present study, the wall-pressure spectrum is obtained using Lee's model [18], taking the inputs from the boundary-layer model implemented in Flighstream. The Corcos model [19] is used to compute the spanwise correlation length as:

$$l_y(\omega) = \frac{\beta U_c}{\omega} \quad (3)$$

where β is a parameter of the model. In the present work, the values $U_c/U_\infty = 0.7$ and $\beta = 1.47$, reported in Ref. [20], respectively, have been adopted. More accurate models accounting

for some frequency dependence have been developed, such as proposed by Efimtsov [21] for the spatial correlation, and Smolyakov [22] for the convection velocity, but haven't been considered in this work.

The trailing-edge noise model developed for an isolated airfoil can be extended for wind turbines by dividing the blade into n strips along the span in order to take into account the spanwise flow variations. Based on the analysis of Lowson [23], Amiet [9] discussed that a dipole source in a circular motion can be approximated as a rectilinear motion if the angular velocity (Ω_{rot}) is much smaller than the source frequencies (ω).

The sound frequency at the observer location, ω_0 is shifted compared to the emitted frequency from the source, $\omega_e(\Psi)$ where $\Psi = \Omega_{rot}t$ is the azimuthal angle. The ratio between is known as the Doppler factor and is given by [24]:

$$\frac{\omega_e}{\omega_0} = 1 + M_t \sin\Psi \sin\Theta \tag{4}$$

where M_t is the Mach number of the source relative to the observer, respectively. The observer angles are defined in Figure 8. The far-field noise is determined by averaging all the possible azimuthal positions of the blade segments and weighting it with the Doppler factor. The formulation is given for a rotating machine with B independent blades and low-solidity, thus the blade-to-blade interaction is assumed negligible:

$$S_{pp}(X, Y, Z, \omega_0) = \frac{B}{2\pi} \int_0^{2\pi} \left(\frac{\omega_e}{\omega_0}\right)^n S_{pp}^{\Psi}(x, y, z, \omega_e) \mathrm{d}\Psi \tag{5}$$

where S_{pp}^{Ψ} is the noise emitted from a source located at Ψ neglecting the Doppler effect and is thus the same as the isolated airfoil given in Eq. (2). The exponent n is defined as 1 for the instantaneous spectrum and 2 for the time-averaged spectrum [25, 26].

2.3.3 Example of aeroacoustic predictions

An example of results is shown in Figure 9 for a DEP configuration with 3 rotors. The broadband and tonal components of the complete system are computed on a half-sphere oriented towards the ground, using the methods described above. The input data are sampled from an unsteady Flightstream simulation, over multiple rotations. For the tonal component, the pressure on the blade surface is sampled over 4 rotations with 60 points per rotation. This initial attempt will be revised after convergence tests of the results. The blade surface is divided into 7 and 2 patches along the span and chord respectively, allowing to take into account the variation of the mean pressure on the surface while keeping compact dipoles. The dipoles, obtained by integration of the pressure over the patches, are injected in formulation (1). Only the first 5 BPFs are considered, keeping in mind that the panel code Flightstream is not resolving turbulence. Only upstream flow uniformities and potential interactions will create unsteady pressure on the blade, resulting in sound production at higher BPFs than the rotor BPF. The sound directivity for the first BPF is shown in Figure 9, with a main radiation lobe oriented in the rotor plane. In the case of trailing-edge broadband noise, the boundary-layer parameters are sampled for 5 strips at 2% chord upstream of the trailing edge. The resulting values are phased-locked averaged with the rotation and used in the trailing-edge wall-pressure model and then in Amiet's formulation. Pressure and suction side values are treated separately. The corresponding far-field sound directivity is shown in Figure 9 at 10 kHz, showing a directivity lobe oriented upstream of the DEP configuration due to the directivity of the aeroacoustic transfer function at high frequencies. By integrating the directivity spheres, resulting sound power levels are obtained, as shown in Figure 9. Those values will be used as objectives for the optimisation.

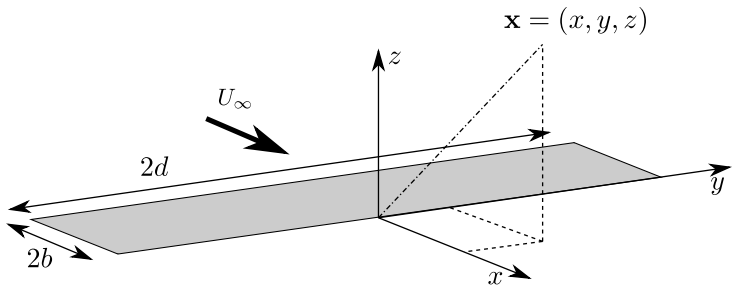


Figure 7: Flat plate representation and coordinate system in Amiet's theory.

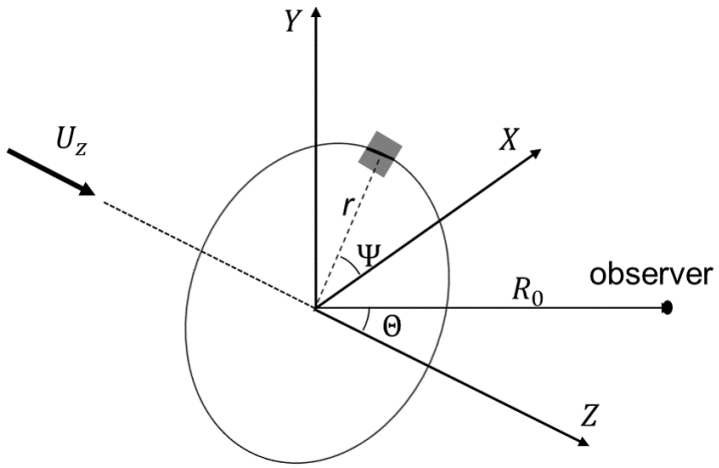


Figure 8: Sketch of the observer and source for a rotating machine.

2.4 Optimizer

The modeFRONTIER [27] optimization suite is used to manage the solver calls, result data and geometrical parameter changes. Different implementations of genetic algorithms and hybrid strategies involving response surface modelling can be found in this package, allowing for flexibility in algorithm selection. Due to the black box nature of the solvers used, gradient-free methods have been employed for the optimization process.

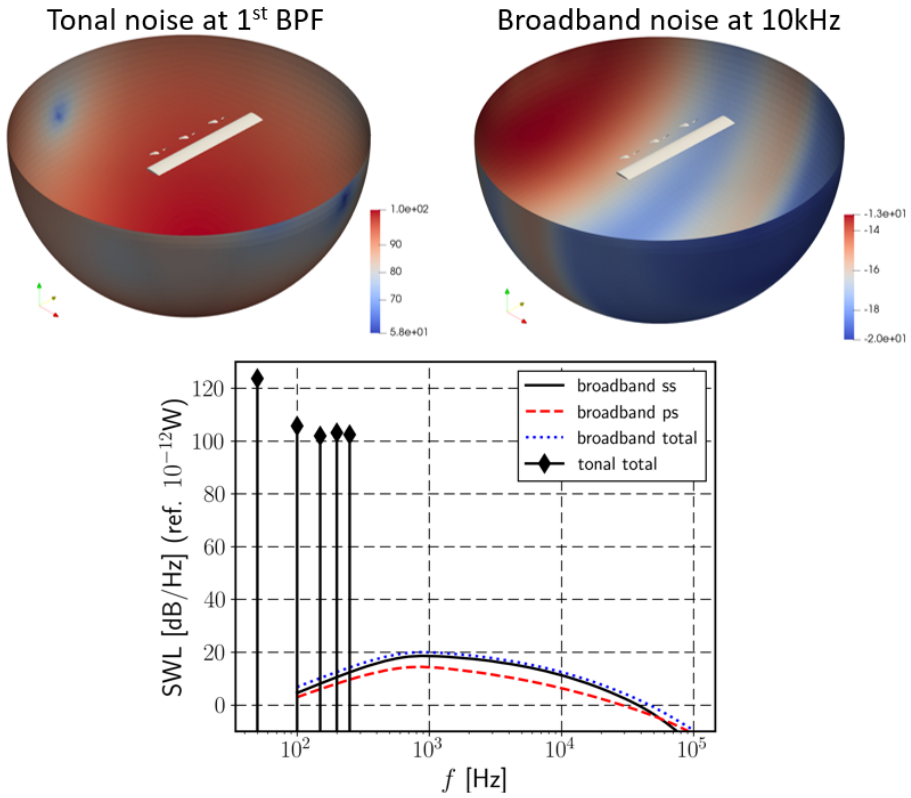


Figure 9: Sound radiated for a 3 rotors DEP configuration

3 Optimization results

3.1 Baseline design

A three-bladed distributed electric propulsion (DEP) propeller has been designed following the methodology introduced by Patterson [28] for the baseline configuration of this optimization process. Chord and twist distributions are plotted in Figure 11. The wing is a 3.5 meter span and 0.95 meter constant chord section of the Pipistrel Sinus aircraft wing. Table 1 contains some parameters of the propeller along with its operating condition.

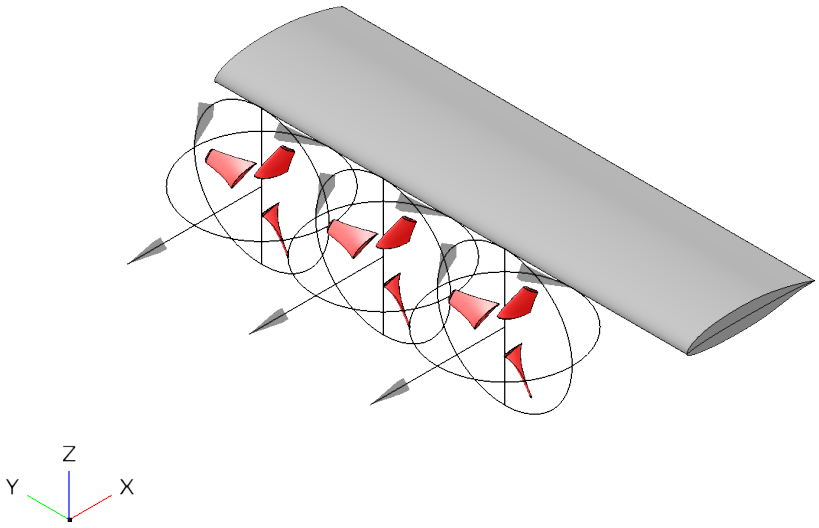


Figure 10: Three-dimensional view of the baseline geometry from *OpenVSP*.

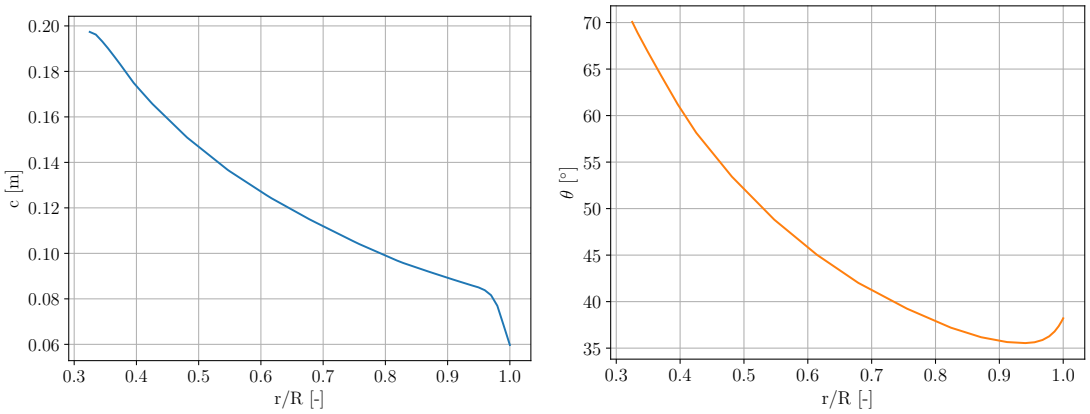


Figure 11: Propeller chord distribution (left) and twist distribution (right).

3.2 Methodology

An optimization process has been run using the framework described in the previous sections. This includes geometry preprocessing through the open source geometry engine *OpenVSP*, panel

R [m]	0.40
r_0 [m]	0.13
Airfoil	MH114
$\theta_{3/4}$ [°]	39.42
Ω [rpm]	4100
α [°]	6.5
v_∞ [m/s]	48

Table 1: Parameters of the DEP propeller and operating point.

method aerodynamics through *FlightStream* and propeller tonal and broadband noise quantification through the *BATMAN*$^\pi$ acoustics toolbox developed by von Karman Institute for Fluid Dynamics, using *modeFRONTIER* as an optimization hypervisor. The four optimization variables are shown in Figure 12 and described in Table 2. Definition of horizontal displacement Δy is reversed for the left and right propellers.

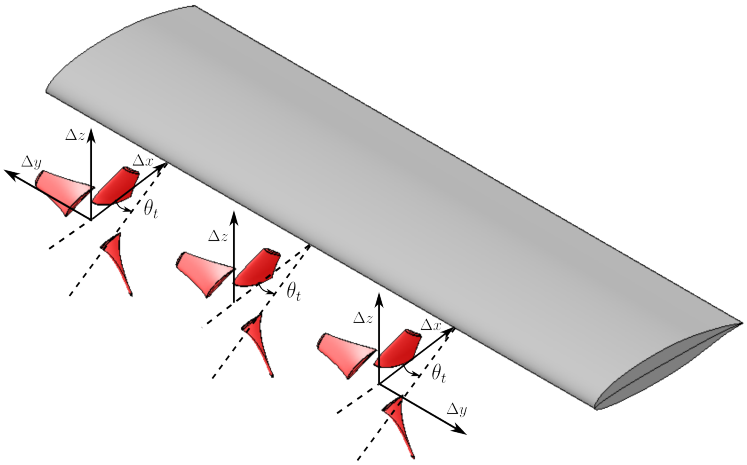


Figure 12: Optimization variables.

Variable name	**Description**	**Minimum value**	**Maximum value**
Δx [m]	Axial displacement/stagger	-0.1	0.1
Δy [m]	Horizontal displacement	-0.09	0.09
Δz [m]	Vertical displacement	-0.2	0.2
θ_t [°]	Propeller tilt angle	0.0	10.0

Table 2: Description of optimization variables.

The objective function to minimize is the sum of broadband OASWL and the mean tonal

SWL at the first 5 blade passing frequencies:

$$f(\mathbf{x}) = OASWL_{bb}(\mathbf{x}) + \frac{1}{5}\sum_{i=1}^{5} SWL^{i}_{tonal} \tag{6}$$

A constraint is introduced, forcing the increase in wing lift divided by the length of the tip-to-tip DEP system $\Delta L/l_{sys}$ to be higher or equal than the one obtained with the baseline configuration ($\Delta x = \Delta y = \Delta z = 0$, $\theta_t = 5°$):

$$\frac{\Delta L}{l_{sys}}(\mathbf{x}) \geq \frac{\Delta L}{l_{sys}}(\mathbf{0}) \tag{7}$$

The *pilOPT* multi-strategy optimization algorithm implemented in the *modeFRONTIER* optimization hypervisor combining evolutionary phases and RSM phases has been chosen for this process.

Acoustic performance is computed over a 15 meter radius semi-sphere centered at the hub of the central propeller. Figure 13 shows a visualization for the baseline configuration, including aerodynamic and acoustic contours.

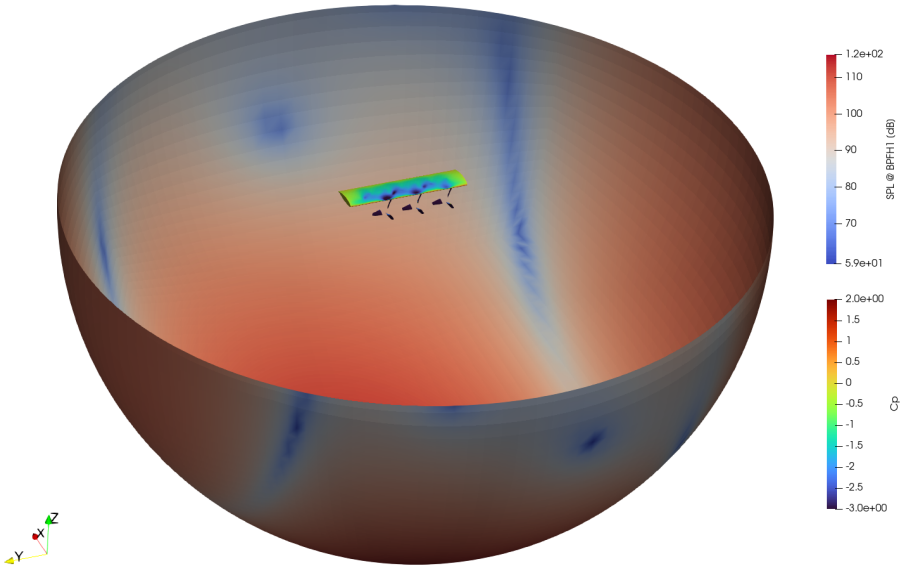


Figure 13: Contour of the results for the baseline configuration. On the sphere, SPL at the first blade passing frequency harmonic. On the wing and propellers, pressure coefficient.

3.3 Results

After 70 optimization iterations using the approach detailed in the previous section, three optimized configurations that improve on the acoustic performance of the baseline system are identified and shown in Table 3.

For the optimized configuration, results show a reduction of 1.99 dB in broadband OASWL and a simultaneous reduction in average mean tonal SWL of 1.21 dB, while achieving a 19.20% higher lift increase per system unit length. This is achieved by moving the two outboard propellers away from the wing's leading edge, further together and vertically up, as well as increasing the tilt angle of the nacelle. This configuration can be observed in Figure 14.

Design	Δx	Δy	Δz	θ_t	SWL_{tot} [dB]	BB [dB]	Tonal [dB]	$\Delta L/l_{sys}$ [N/m]
Baseline	0.0	0.0	0.0	5.0	180.61	60.61	120.00	329.29
Optimized	-0.099	0.089	0.2	10.0	**177.39**	58.60	118.79	392.52
Opt. broadband	-0.1	0.09	0.2	10.0	177.58	**58.46**	119.1	382.02
Opt. tonal	-0.1	-0.085	0.15	10.0	177.82	59.48	**118.34**	543.61

Table 3: Resulting optimized configurations. SWL_{tot} is the objective function value, *BB* refers to broadband OASWL and *Tonal* refers to the averaged SWL at the first 5 blade passing frequencies, as shown in Equation 6.

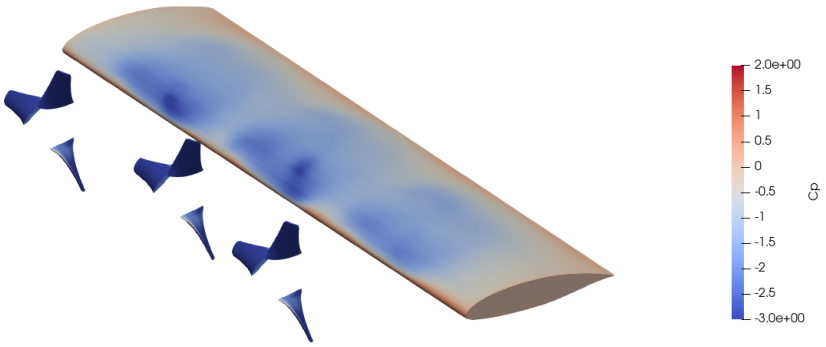


Figure 14: Optimized configuration with pressure coefficient contours.

The next configuration, named *optimized - broadband* in Table 3, shows the lowest broadband OASWL at 58.46 dB. However, geometrically the configuration is almost identical to that of the previous case and these small differences are likely to be due to numerical errors.

A third configuration with the best tonal noise behavior is identified. The main difference with the previous two is a lower vertical offset for the three propellers and a negative Δy displacement, pulling the propellers together. This results in a decrease of 1.66 dB on the mean SWL at the first five blade passing frequency harmonics.

Figure 15 shows the broadband and tonal noise characteristics of the baseline system, optimized and optimized-tonal configurations. The configuration with lowest broadband OASWL has been omitted due to similar spectrum to the optimized one and worse convergence. Over the baseline, the optimized configuration improves the SWL over the whole spectrum for broadband noise while the configuration optimized for tonal noise shows high values close to lower frequencies. Regarding tonal noise, the optimized configuration shows a higher improvement at the first BPFH while the one optimized for tonal noise improves further on higher harmonics.

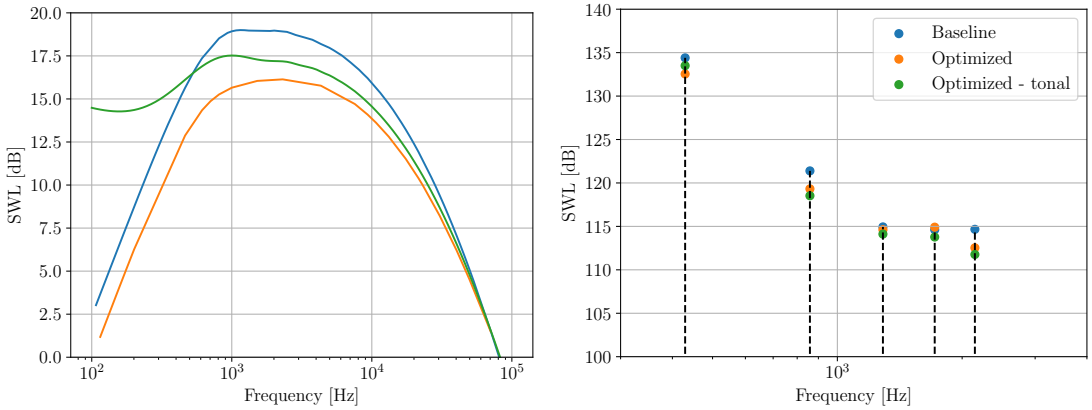


Figure 15: Broadband noise spectrum (left) and tonal SWL values at different BPFH (right) for the optimized configurations.

4 Conclusions

A framework for aeroacoustic optimization has been established and run to improve the aeroacoustic behavior of a DEP system by altering the position of the propellers over the wing. It does so through a low fidelity aerodynamic model and the $BATMAN^{\pi}$ acoustics solver by VKI.

Results show meaningful improvement in noise characteristics where a reduction of 1.99 dB in broadband OASWL and 1.21 dB in average tonal SWL at the first 5 blade passing frequency harmonics was achieved. This represents a useful tool-chain in design stages due to the low computational cost and basic amount of information needed.

Some areas of improvement include running the optimizer for more iterations: in this work, only 70 iterations were performed due to time constraints, hence a better result could be achieved with a longer optimization run. The nacelles are also not modelled due to possible instabilities with the propeller panel wakes, and they may have some influence on the aerodynamic performance of the system.

References

[1] Stephen A Rizzi, Daniel L Palumbo, Jonathan Rathsam, Andrew W Christian, and Menachem Rafaelof. Annoyance to noise produced by a distributed electric propulsion high-lift system. In *23rd AIAA/CEAS Aeroacoustics Conference*, page 4050, 2017.

[2] Hyun D Kim, Aaron T Perry, and Phillip J Ansell. A review of distributed electric propulsion concepts for air vehicle technology. In *2018 AIAA/IEEE Electric Aircraft Technologies Symposium (EATS)*, pages 1–21. IEEE, 2018.

[3] Athanasios Synodinos, Rod Self, and Antonio Torija. Preliminary noise assessment of aircraft with distributed electric propulsion. In *2018 AIAA/CEAS Aeroacoustics Conference*, page 2817, 2018.

[4] Scott W Ashcraft, Andres S Padron, Kyle A Pascioni, Gary W Stout Jr, and Dennis L Huff. Review of propulsion technologies for n+ 3 subsonic vehicle concepts. 2011.

[5] Robert A. McDonald. Advanced Modeling in OpenVSP. *16th AIAA Aviation Technology, Integration, and Operations Conference*, 2016.

[6] Robert A. McDonald and James R. Gloudemans. Open Vehicle Sketch Pad: An Open Source Parametric Geometry and Analysis Tool for Conceptual Aircraft Design. *AIAA SCITECH 2022 Forum*, 2022.

[7] Vivek Ahuja and Roy Hartfield. Predicting the Aero Loads Behind a Propeller in the Presence of a Wing Using Flightstream. *15th AIAA Aviation Technology, Integration, and Operations Conference*, 2015.

[8] Erik D. Olson and Cindy W. Albertson. Aircraft High-Lift Aerodynamic Analysis Using a Surface-Vorticity Solver. *54th AIAA Aerospace Sciences Meeting*, 2016.

[9] R.K. Amiet. Noise due to turbulent flow past a trailing edge. *Journal of Sound and Vibration*, 47(3):387–393, aug 1976.

[10] Michel Roger and Stéphane Moreau. Back-scattering correction and further extensions of Amiet's trailing-edge noise model. Part 1: theory. *Journal of Sound and Vibration*, 286(3):477–506, 2005.

[11] Stewart Glegg and William Devenport. *Aeroacoustics of low Mach number flows: fundamentals, analysis, and measurement*. Academic Press, 2017.

[12] Michel Roger. Aeroacoustics of installed propellers. In *Aircraft Electric Propulsion*, number LS 2019-02 in VKI Lecture Series. von Karman Institute, Rhode-St-Genèse, 2019.

[13] JE Ffowcs Williams and DL Hawkings. Theory relating to the noise of rotating machinery. *Journal of Sound and Vibration*, 10(1):10–21, 1969.

[14] Michel Roger and Stéphane Moreau. Tonal-Noise Assessment of Quadrotor-Type UAV Using Source-Mode Expansions. *Acoustics*, 2(3):674–690, September 2020.

[15] M. E. Goldstein. Aeroacoustics. 1976.

[16] M. Roger. *Aeroacoustics of installed propellers*. Number 2019-02 in von Karman Institute Lecture Series. von Karman Institute for Fluid Dynamics, 2019.

[17] R.K. Amiet. Effect of the incident surface pressure field on noise due to turbulent flow past a trailing edge. *Journal of Sound and Vibration*, 57(2):305–306, 1978.

[18] Seongkyu Lee. Empirical wall-pressure spectral modeling for zero and adverse pressure gradient flows. *AIAA Journal*, 56(5):1818–1829, 2018.

[19] G. M. Corcos. The structure of the turbulent pressure field in boundary-layer flows. *Journal of Fluid Mechanics*, 18(03):353, mar 1964.

[20] Yannick Rozenberg, Gilles Robert, and Stéphane Moreau. Wall-pressure spectral model including the adverse pressure gradient effects. *AIAA Journal*, 50(10):2168–2179, 2012.

[21] BM Efimtsov. Characteristics of the field of turbulent wall pressure-fluctuations at large Reynolds-numbers. *Soviet Physics Acoustics-USSR*, 28(4):289–292, 1982.

[22] A. V. Smol'yakov. A new model for the cross spectrum and wavenumber-frequency spectrum of turbulent pressure fluctuations in a boundary layer. *Acoustical Physics*, 52(3):331–337, 2006.

[23] M. V. Lowson. The sound field for singularities in motion. *Proceedings of the Royal Society A: Mathematical, Physical and Engineering Sciences*, 286(1407):559–572, aug 1965.

[24] Stephane Moreau and Michel Roger. Competing broadband noise mechanisms in low-speed axial fans. *AIAA Journal*, 45(1):48–57, 2007.

[25] S. Sinayoko and J. Hurault. On predicting wind turbine noise and amplitude modulation using amiet's theory. In *Conference: International Conference on Wind Turbine Noise*, 2015.

[26] S. Sinayoko, M. Kingan, and A. Agarwal. Trailing edge noise theory for rotating blades in uniform flow. *Proceedings of the Royal Society A: Mathematical, Physical and Engineering Sciences*, 469(2157):20130065–20130065, 2013.

[27] L. Nardin, K. Sorensen, S. Hitzel, and U. Tremel. modeFRONTIER, a Framework for the Optimization of Military Aircraft Configurations. 2009.

[28] Michael D. Patterson. Conceptual design of high-lift propeller systems for small electric aircraft. 2016.